

Seismogenic model of the 2023 M_W 5.5 Pingyuan earthquake in North China Plain and its tectonic implications

Shiguang Wang, Libo Han, Junju Xie, Liping Fan, Xiang Huang, Jinmeng Bi, Hongfeng Yang, Lihua Fang

Citation: Wang SG, Han LB, Xie JJ, Fan LP, Huang X, Bi JM, Yang HF, Fang LH (2024). Seismogenic model of the 2023 M_W 5.5 Pingyuan earthquake in North China Plain and its tectonic implications. *Earthquake Science*, 37(6): 499–513, doi: 10.1016/j.eqs.2024.06.008

View online: <http://www.equseci.org.cn/article/doi/10.1016/j.eqs.2024.06.008>

Related articles that may interest you

Crustal velocity, density structure, and seismogenic environment in the southern segment of the North–South Seismic Belt, China
[Earthquake Science. 2021, 34\(6\), 471 https://doi.org/10.29382/eqs-2021-0052](#)

S-wave velocity structure in Tangshan earthquake region and its adjacent areas from joint inversion of receiver functions and surface wave dispersion
[Earthquake Science. 2020, 33\(1\), 42 https://doi.org/10.29382/eqs-2020-0042-05](#)

Double-difference tomography of P- and S-wave velocity structure beneath the western part of Java, Indonesia
[Earthquake Science. 2019, 32\(1\), 12 https://doi.org/10.29382/eqs-2019-0012-2](#)

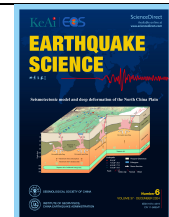
Three-dimensional crustal P-wave velocity structure in the Yangbi and Eryuan earthquake regions, Yunnan, China
[Earthquake Science. 2021, 34\(4\), 358 https://doi.org/10.29382/eqs-2021-0025](#)

Stress drop assessment of the August 8, 2017, Jiuzhaigou earthquake sequence and its tectonic implications
[Earthquake Science. 2020, 33\(4\), 161 https://doi.org/10.29382/eqs-2020-0161-01](#)

Three-dimensional velocity structure around the focal area of the 2021 M_S 6.4 Yangbi earthquake
[Earthquake Science. 2021, 34\(5\), 399 https://doi.org/10.29382/eqs-2021-0033](#)



Follow Earthq Sci WeChat public account for more information



Article

Seismogenic model of the 2023 M_W 5.5 Pingyuan earthquake in North China Plain and its tectonic implications

Shiguang Wang¹, Libo Han¹, Junju Xie¹, Liping Fan¹, Xiang Huang¹, Jimmeng Bi², Hongfeng Yang^{3,✉} and Lihua Fang^{1,4,✉}

¹ Institute of Geophysics, China Earthquake Administration, Beijing 10081, China

² Tianjin Earthquake Agency, Tianjin 300201, China

³ Earth System Science Programme, The Chinese University of Hong Kong, Shatin, Hong Kong 999077, China

⁴ Beijing Baijiatuan Earth Science National Observation and Research Station, Beijing 100095, China

Key points:

- The aftershocks of the M_W 5.5 Pingyuan earthquake trends NE with a total length of ~9 km and dips NW at an angle of ~60°.
- The observed horizontal PGAs and PGVs generally ranges between 200–300 cm/s² and 10–20 cm/s, resulting a significant near-field saturation phenomenon within a 20-kilometer range.
- A blind fault between the Guantao fault and the Lingxian-Yangxian fault was responsible for the generation of the Pingyuan earthquake.

ABSTRACT

The 6 August 2023 M_W 5.5 Pingyuan earthquake is the largest earthquake in the central North China Plain (NCP) over the past two decades. Due to the thick sedimentary cover, no corresponding active faults have been reported yet in the epicenter area. Thus, this earthquake presents a unique opportunity to delve into the buried active faults beneath the NCP. By integrating strong ground motion records, high-precision aftershock sequence relocation, and focal mechanism solutions, we gain insights into the seismotectonics of the Pingyuan earthquake. The aftershocks are clustered at depths ranging from 15 to 20 km and delineate a NE-SW trend, consistent with the distribution of ground motion records. A NE-SW nodal plane (226°) of the focal mechanism solutions is also derived from regional waveform inversion, suggesting that the mainshock was dominated by strike-slip motion with minor normal faulting component. Integrating regional geological data, we propose that an unrecognized fault between the NE-SW trending Gaotang and Lingxian-Yangxin faults is the seismogenic fault of this event. Based on the S-wave velocity structure beneath the NCP, this fault probably extends into the lower crust with a high angle. Considering the tectonic regime



Production and Hosting by Elsevier on behalf of KeAI

© 2024 The Authors. Publishing services by Elsevier B.V. on behalf of KeAi Communications Co. Ltd. This is an open access article under the CC BY-NC-ND license (<http://creativecommons.org/licenses/by/4.0/>).

Peer review under the responsibility of Institute of Geophysics, China Earthquake Administration.

✉ Corresponding author. Yang HF, email: hyang@cuhk.edu.hk; Fang LH, email: flh@cea-igp.ac.cn

Article history:

Received 17 January 2024

Received in revised form 14 March 2024

Accepted 7 April 2024

Available online 23 April 2024

<https://doi.org/10.1016/j.eqs.2024.06.008>

and stress state, we speculate that the interplay of shear strain between the Amurian and South China blocks and the hot upwelling magma from the subducted paleo Pacific flat slab significantly contributed to the generation of the Pingyuan earthquake.

Keywords: Pingyuan earthquake; aftershock relocation; focal mechanism; S-wave velocity structure; North China Plain

Citation: Wang SG, Han LB, Xie JJ, Fan LP, Huang X, Bi JM, Yang HF and Fang LH (2024). Seismogenic model of the 2023 M_W 5.5 Pingyuan earthquake in North China Plain and its tectonic implications. *Earthq Sci* 37(6): 499–513, doi: 10.1016/j.eqs.2024.06.008.

1. Introduction

On August 6th, 2023, an M_W 5.5 Pingyuan earthquake occurred in Pingyuan County, Shandong Province, the central area of the North China Plain (NCP). The catalog location was at 37.16°N and 116.34°E (Zhang Z et al., 2024), and had a focal depth of 10 km, as reported by the China Earthquake Networks Center (CENC, <https://news.ceic.ac.cn/CC20230806023360.html>). Due to the presence of a thick sedimentary cover in the area and consequent amplification effect, the earthquake caused significant ground shaking, resulting in 24 injuries and 213 collapsed houses. This event marked the largest earthquake in the NCP over the past 20 years (<http://www.ceic.ac.cn/history>). According to the intensity map released by China Earthquake Administration, the highest intensity reached VII within an approximate area of 22 km² (<https://www.cea.gov.cn/cea/xwzx/fzjzyw/5736905/index.html>).

As one of the most densely populated regions in China, the NCP is also highly susceptible to earthquake activities and hazards. According to historical and instrumental records (Liu M et al., 2011; Zhang PZ et al., 2013; Zhang YG et al., 2018; Yin XF et al., 2020), there have been 8 earthquakes with magnitudes larger than M 7.0 in the region. Notably, the 1679 M 8.0 Sanhe-Pinggu earthquake occurred only 40 km east of Beijing (Yu ZY et al., 2019), leading to 45,500 deaths and countless houses damaged, including the Forbidden City (Jiang PF, 2022). The most recent major earthquakes in the area were the 1966 M 7.2 Xingtai earthquake and the 1976 M 7.8 Tangshan earthquake, resulting in deaths of over 8,000 and 240,000 people, respectively (Xu J et al., 1996; Guo H et al., 2011; Guo H and Zhao JX, 2019). Prior to these two events, limited information was available concerning the seismicity and active faults in the NCP (Zhang ZL et al., 1980; Liu M et al., 2011; Yu ZY et al., 2019), due to the substantial sedimentary thickness (Wang CY et al., 2017; Huang X et al., 2023). Furthermore, no moderate earthquakes and active faults in the Holocene have been identified within 60 km of the 2023 Pingyuan mainshock, hindering further investigation into the earthquake activity in the neighboring regions and central NCP. Therefore,

this event presents a valuable opportunity to study the regional seismotectonics.

Shortly after this event, preliminary analysis of source parameters and inversion of the rupture process have been reported quickly (Dai DQ and Xi N, 2023; Zhang YX et al., 2023). Zhang Z et al. (2024) have also relocated early aftershocks and determined focal mechanism solution of the mainshock. Such rapid reports provided valuable information about the seismic characteristics of the Pingyuan earthquake. However, the seismogenic fault and implications are still unclear due to the relatively few aftershocks and fault structure analysis.

To understand the earthquake fault and mechanism of the 2023 M_W 5.5 Pingyuan earthquake, we conduct a relocation of aftershocks from August 6th to 17th, 2023, in which more aftershocks are detected. Additionally, we invert the focal mechanism solution of the mainshock using data from local and regional seismic networks. Furthermore, we integrate regional S-wave tomographic images to jointly analyze the detailed geometry of the seismogenic fault. We then discuss the fault structures in the source area and the seismotectonic environment in the central NCP.

2. Tectonic setting

The Pingyuan earthquake occurred in the central NCP (Figure 1a), geologically defined as the Eastern North China Craton (NCC). During the Early Cretaceous (~135–115 Ma, Zhu RX et al., 2012; Qiu HB et al., 2023), the NCC underwent significant lithosphere thinning accompanied by intensive magmatism (Zhu RX et al., 2012; Zhang SH et al., 2014), widespread NNE-SSW striking rifts (Meng QR, 2003) and many metamorphic core complexes (Wang T et al., 2011; Zhu G et al., 2015). In the Early Cenozoic (~50–35 Ma), the NCC experienced a second stage of crustal extension and the heat flow further destroyed its middle crust (Xu W et al., 2018, 2019). As a result, the lithosphere of the NCC has been reduced by about 100 km, leading to its current unstable state (Gao S et al., 2002; Lin W et al., 2008).

Since the Neocene (~23 Ma), the NCP has primarily

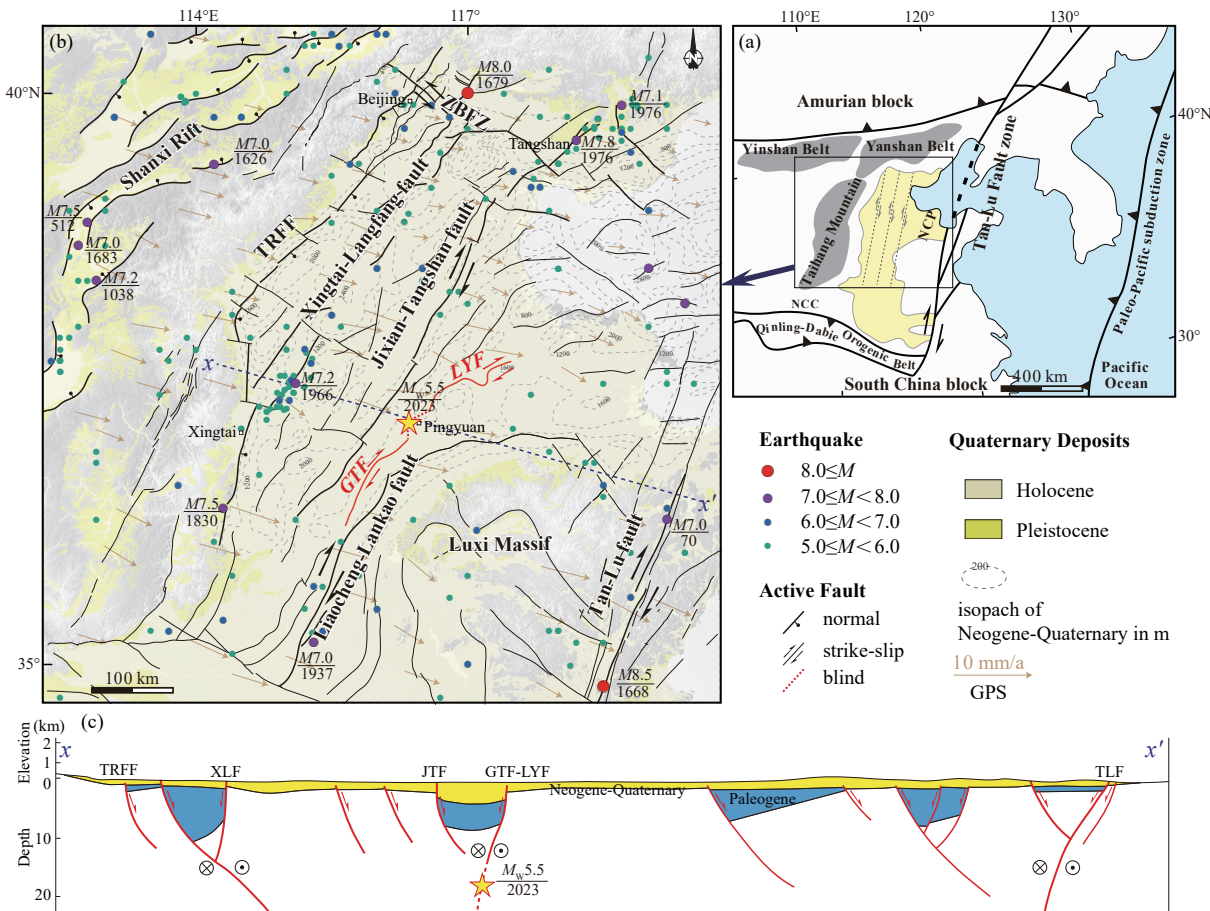


Figure 1. Seismotectonic and present structure of the North China Plain (NCP). (a) Tectonic subdivisions and interior deformation of NCP. (b) Tectonic map of NCP with horizontal GPS velocities (Zheng G et al., 2017), historical earthquakes of $M \geq 5.0$ (CENC), and active faults (modified after Zhang YG et al., 2018), location in (a). (c) Geological profiles in NCP showing the geometrical features of active faults, profile in (b). The geometrical characteristics of faults are based on Li SZ et al. (2012). NCC: North Chian Craton; TRFF: Taihang range front fault; ZBFZ: Zhangjiakou-Bohai fault zone; XLF: Xingtai-Langfang fault; JTF: Jixian-Tangshan fault; GTF: Gaotang fault; LYF: Lingxian-Yangxin fault; TLF: Tan-Lu fault.

been influenced by post-rift transtension, resulting in extensive strata deposition with a cumulative thickness of around 3–4 km (Huang X et al., 2023; Figure 2). The Neocene sedimentary layer in the region consists of the Guantao Formation (Ng) and the Minghuazhen Formation (Nm^L–Nm^U) from bottom to up. These formations are characterized by conglomerate at the bottom, overlain by moderately thick sandstone, siltstone, and mudstone layers (Figure 2). During the Quaternary, the main strata in the NCP is the Pingyuan Formation, which is predominantly composed of thin layers of siltstone and mudstone, with a thickness reaching approximately 1000 m (Figure 2).

Known for strong seismic activities, the NCP is bounded by various geological features. The Tan-Lu fault zone (TLFZ) lies to the east, while the Taihang mountain range is found to the west. To the north, the region is bounded by the Yanshan belt and the Zhangjiakou-Bohai fault zone (ZBFZ), while the Luxi Massif borders it to the

south (Figure 1a and 1b). Within this region, three major right-lateral strike-slip NNE-trending faults play a significant role in accommodating present deformation. These faults are the Xingtai-Langfang fault (XLF), Jixian-Tangshan fault (JTF), and Liaocheng-Lankao fault (LLF) (Figure 1b and 1c). North of LLF, the Gaotang fault (GTF) and Lingxian-Yangxin fault (LYF) are the two main faults that activated during the Late Pleistocene around the epicentral area. The GTF is situated in the of Pingyuan County, with a strike of 30°–40° and a dip angle of 60°–80°, spanning ~135 km. Trending NE-ENE with a dip angel of 60°–70°, the LYF stretches about 120 km in the northeast of Pingyuan County, and curves in a convex arc towards southeast in its northern section (Ma SZ, 2007). Both of GTF and LYF are right-lateral strike slip faults with normal components (Figure 1b and 1c).

Historical records indicate that 8 devastating earthquakes with magnitudes of $M \geq 7.0$ have been

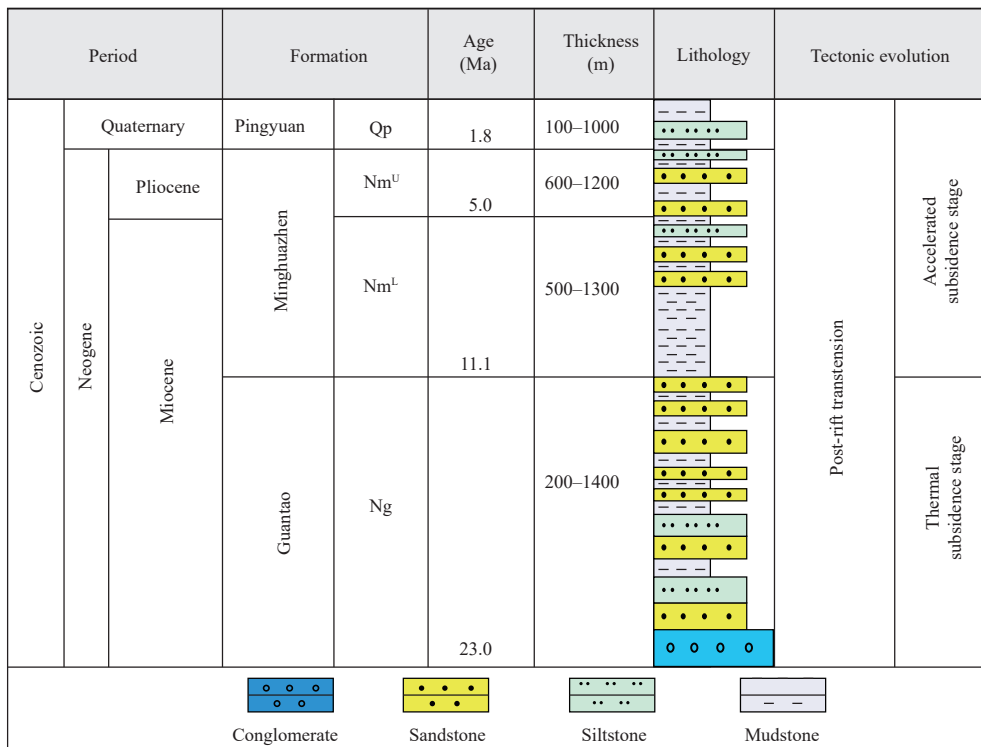


Figure 2. Strata sequences of the NCP showing the ~4 km thickness of Neogene-Quaternary sedimentary in central NCP (revised from Yu FS and Koyi, 2016; Wang GZ et al., 2022).

associated with these faults. Among them, six earthquakes occurred in the last 344 years. After the Sanhe-Pinggu $M8.0$ earthquake in 1679, the NCP experienced a relatively quiet period of over 100 years. Only one significant earthquake, the 1830 $M7.5$ Cixian earthquake, occurred during the nineteenth century. However, from 1937 to 1976, the region witnessed a period of intensive seismic activity, including four major earthquakes: the 1937 Heze $M7.0$ earthquake, the 1966 Xingtai $M7.2$ earthquake, the 1976 Tangshan $M7.8$ earthquake, and the 1976 Luanxian $M7.1$ earthquake.

3. Spatial distribution characteristics of strong ground motion

We collected 1 349 strong motion station records of the Pingyuan M_W 5.5 mainshock that were observed by the National Intensity Rapid Report and Earthquake Early Warning Network of China. The records with low signal-to-noise ratios or anomalous waveforms were excluded. A total of 965 three-component acceleration records were selected for this study. We applied baseline correction and causal-bandpass Butterworth filtering (0.1–100 Hz) to these records. Subsequently, we integrated the records to obtain the velocity and displacement time histories.

Figure 3 shows the spatial distribution of observed horizontal ground motion intensity measures (IMs) in the near-field, including peak ground acceleration (PGA), peak ground velocity (PGV) and spectral accelerations (SAs) at different periods. The horizontal IMs are calculated as the geometric mean of the East-West and North-South components. Despite the relatively small magnitude of the Pingyuan earthquake, the spatial distribution of near-field ground motion exhibits distinct features of rupture directivity effect (Figure 3a-d). In the rupture forward region, northeast of the epicenter, large IMs values (shown as red to green triangles) are observed in a much wider spatial region. With similar epicentral distance, the observed IMs in the northeast of the epicenter are higher and attenuate slowly relative to the southwest of the epicenter, particularly in terms of PGV and long-period SAs at 1.0 and 3.0 s. We attribute such a pattern to the source rupture directivity and strike-slip faulting mechanism and strike-slip faulting mechanism. Meanwhile, we found that, compared with Kumamoto M_w 7.0 earthquake (Xie JJ et al., 2017) with the strike-slip faulting mechanism at periods above 5.0 s, the directivity effects in the Pingyuan earthquake are relatively minor, likely due to the earthquake's relatively small magnitude. Consequently, the directivity effect primarily influences PGV and long-period SAs of 1.0 s to 3.0 s (Figure 3c, d). During low-

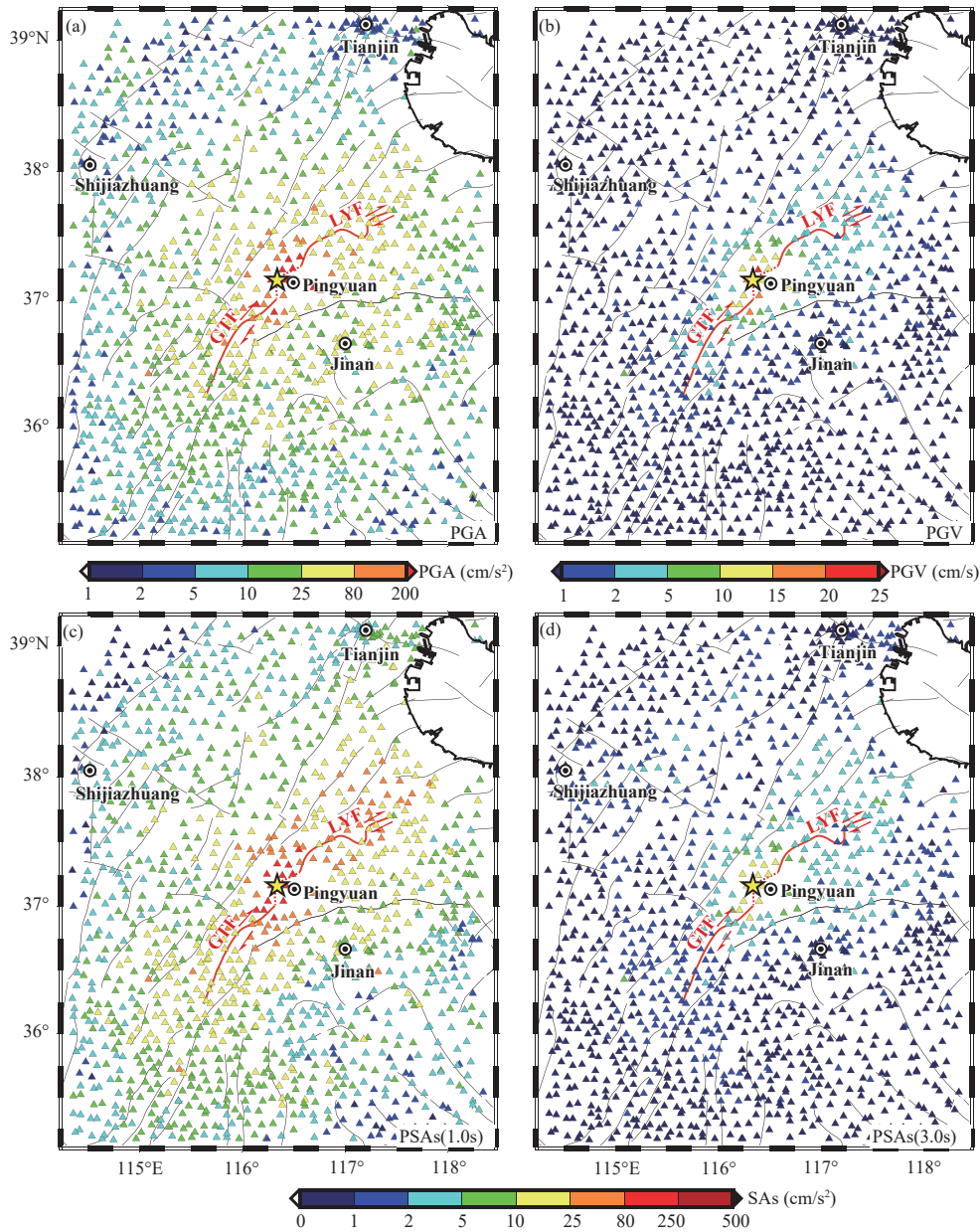


Figure 3. Spatial distribution of observed horizontal PGA (a), PGV (b) and the PSAs at different periods (c–d) during the Pingyuan $M_w5.5$ mainshock.

magnitude earthquakes, the rupture directivity effects on ground motion are generally weak and hard to observe (Xie JJ et al., 2023). The ability of capturing clear directivity effects during this $M_w5.5$ earthquake benefited from the dense ground motion observatories in the area.

We investigated the attenuation of horizontal PGA, PGV, and SAs with epicentral distance during the $M_w5.5$ mainshock. The observed IMs were also compared with the predictions from the ground motion models of shallow crustal earthquakes (Figure 4). Our results reveal a significant near-field saturation phenomenon within 30 km, with observed horizontal PGAs and PGVs generally

ranging between 200–300 cm/s² and 10–20 cm/s, respectively, larger than model predictions (Figure 4). Such near-field deviation from empirical models was also found in numerical simulations considering dynamic rupture process (Yao SL and Yang HF, 2023). The attenuation of PGA, PGV and SAs with distance generally indicates a three-stage decay pattern. Between 50 and 100 km from the epicenter, observed ground motion peaks and SAs demonstrate a scattered and slowly decaying trend, which may be caused by the amplification effects of the regional thick Quaternary sediments.

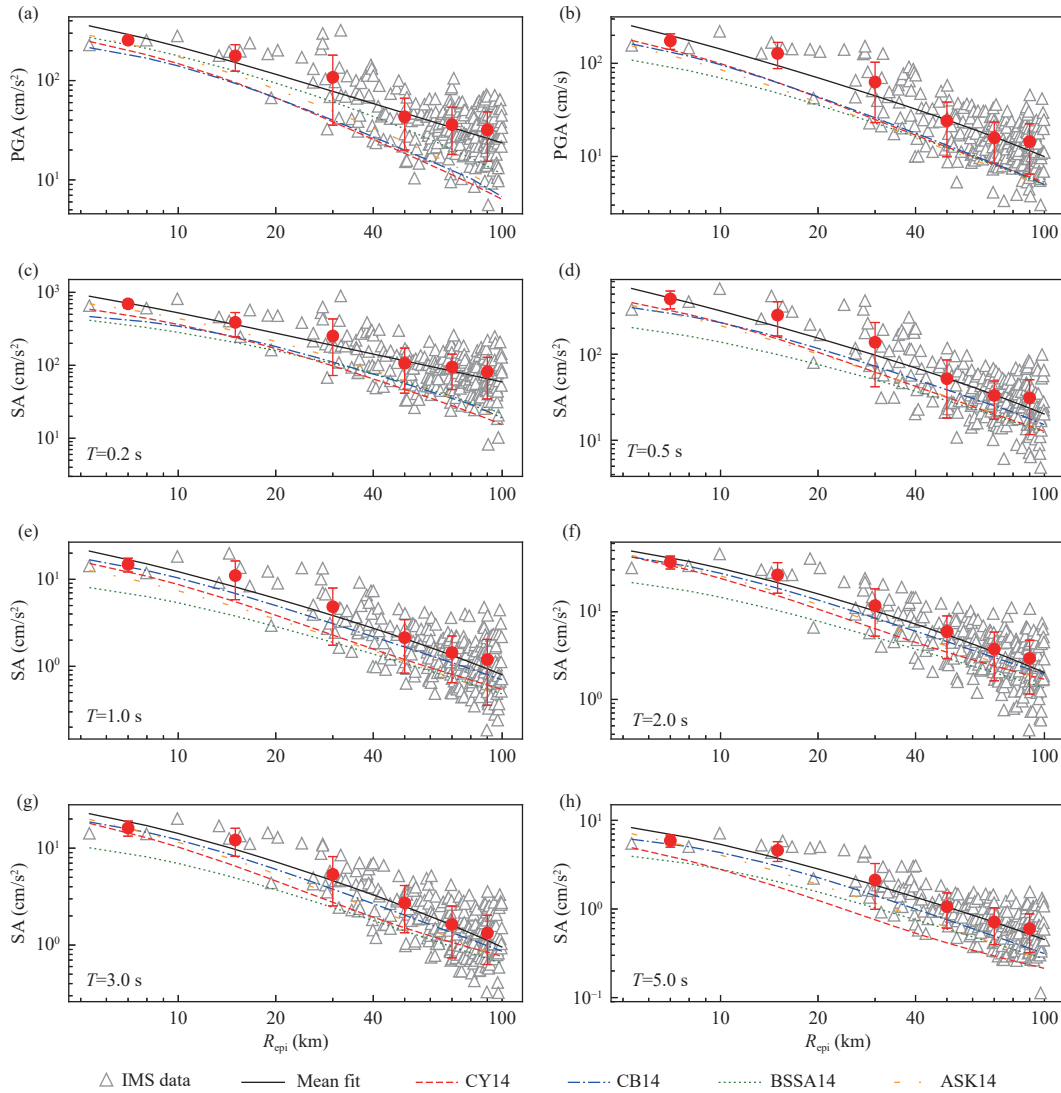


Figure 4. Attenuation of observed PGA (a), PGV (b) and SAs at various periods (c–h) with epicentral distance and the comparison with predictions from the ground motion models of CY14 (Chiou and Youngs, 2014), CB14 (Campbell and Bozorgnia, 2014), BSSA14 (Boore et al., 2014) and ASK14 (Abrahamson et al., 2014).

4. Analysis of earthquake sequence

4.1. Relocation of aftershocks and earthquake sequence parameters

Between the mainshock occurrence and 4:00 am on August 17th, 2023 (Beijing time), a total of 299 events were processed by the Real-time Intelligent Seismic Processing System (RISP), as detailed by Liao SR et al. (2021). RISP detected earthquakes and picked phase arrivals with PhaseNet (Zhu WQ and Beroza, 2019). The earthquake bulletins contain 3,499 P-wave arrivals and 4,610 S-wave arrivals. This catalog, in contrast to conventional ones, encompasses a greater number of small magnitude earthquakes and weak signals, thereby enabling

a more intricate depiction of the fault geometry. After screening by location residuals, detection probabilities, and number of phase arrivals, a subset of 260 events, with 1,972 P-wave arrivals, and 1,171 S-wave arrivals were selected for relocation using the double-difference relocation method (Waldbauer and Ellsworth, 2000), which has been widely applied in the earthquake sequence in China (Fang LH et al., 2015; Fan LP et al., 2022; Zhao C et al., 2022; Zhang L et al., 2023).

The relocation of the aftershock sequence drew upon data from 74 seismic stations, resulting in robust azimuthal coverage (Figure 5a). To enhance precision, we adapted the velocity model based on deep seismic sounding (Duan YH et al., 2016). The average location uncertainties in the east-west, north-south, and vertical directions were 0.38 km, 0.33 km, and 0.51 km, respectively. Additionally, the

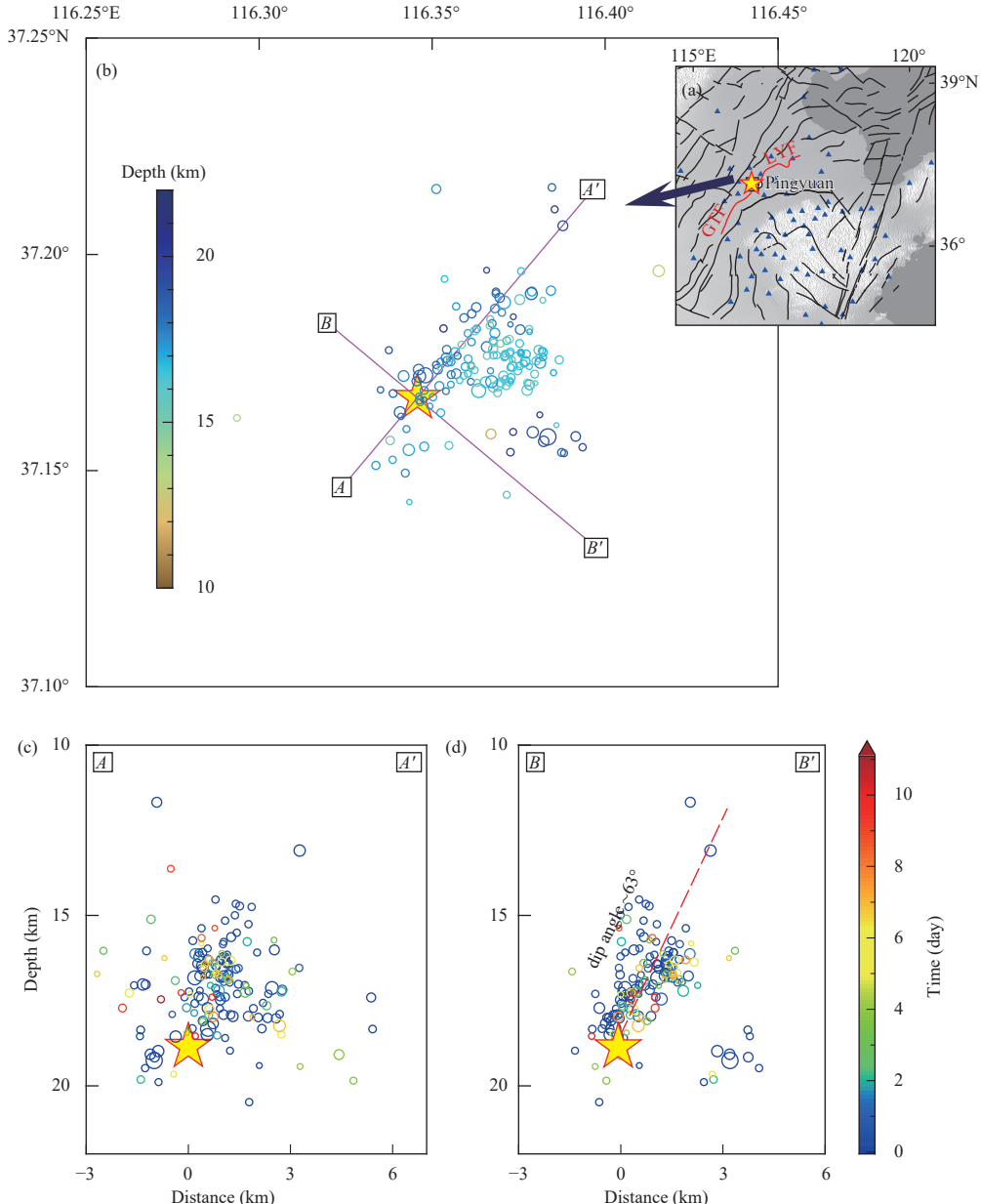


Figure 5. The distribution of relocated aftershocks. (a) The distribution of stations used for relocation; (b) the epicentral distribution of aftershocks, the colors are coded by depth; (c) depth profile of the events along the AA' section, with colors coded by time since the origin time of the mainshock; (d) depth profile of the events along the BB' section and the inferred fault plane (the red dashed line). The red pentagram represents the mainshock, the circles represent aftershocks and the blue triangles represent seismic stations.

average residual time was 0.017 seconds, providing clarity in delineating the seismogenic fault morphology. The relocated 165 events exhibit a trend of N40°E and span a total length of approximately 9 km. These events are concentrated within the 15 km to 20 km range (Figure 5b and 5c). Notably, the aftershocks predominantly cluster to the northeast of the epicenter and occur at shallower depths than the mainshock. The fault-normal profile reveals that the seismogenic fault dips northwest at an approximate

angle of 63° (Figure 5d).

To better reflect the changing characteristics of sequence parameters, we utilized the Omi-R-J model (Omi et al., 2013) that fully considers small earthquake information to perform continuous and sliding parameter fitting on the $M_w 5.5$ Pingyuan earthquake sequence. The Omi-R-J model is a combination of the traditional R-J model (Reasenberg and Jones, 1989) and the OK1993 model (Ogata and Katsura, 1993) of magnitude-frequency

relation in the form of continuous function. Omi et al. (2013) used the expression of the detection rate function provided by Ogata and Katsura (1993) to describe detection degrees of the incomplete parts of seismic records. The sequence parameters can be calculated using the maximum likelihood method.

The function of aftershock intensity of magnitude M at time t in the earthquake sequence can be written as

$$\lambda(t, M) = \frac{k}{(t+c)^p} 10^{-bM}, \quad (1)$$

where k is a normalized positive constant, which determines the expected number of aftershocks triggered by M events. p represents the attenuation degree of the sequence, with its value positively correlated with the speed of attenuation. c represents a small constant. b represents the stress accumulation level, which is one of the important parameters in probabilistic seismic hazard analysis (Wiemer and Katsumata, 1999).

The earthquake events detected by RISP are 2.5 times that of manually processed earthquakes. The aftershocks are mostly distributed below $M_L 3.0$, especially in $M_L 1.0\text{--}1.9$, and the magnitude of completeness was reduced from $M_L 2.4$ to $M_L 2.0$ in the early post-earthquake stage. The events detected by RISP in the early stage after the earthquake are obviously more than those detected by conventional catalogue, and the difference between them gradually decreases as the sequence continued. In the model, the starting time was set at 0.10 days after the mainshock and incrementally stepped by 0.10 days until reaching 12.00 days of the sequence. Subsequently, sliding fitting was performed for 120 time periods.

In the early stages of the earthquake sequence, the p value showed a certain range of variation, gradually increasing from 1.18 to 1.37, and then decreasing to around 1.19 based on conventional catalogue (Figure 6a). While the parameter p value calculated from the catalogue detected by the RISP changes between 1.15 and 1.29, and finally tends to 1.22 (Figure 6b). This p value was higher than the average value (0.98) and the median value (1.02) calculated for the earthquake sequence with $M \geq 6.0$ in the Chinese mainland (Bi JM et al., 2022), indicating rapid decay of this earthquake sequence. The parameter b remained relatively constant at approximately 0.90 (Figure 6c and d), which was higher than the average value (0.85) and the median value (0.83) observed for earthquakes with magnitudes above 6.0 in the Chinese mainland (Bi JM et al., 2022), suggesting significant stress in the focal area and a relatively low differential stress level.

By comparing the calculation results of the two types of catalogues, it is shown that the sequence parameters b

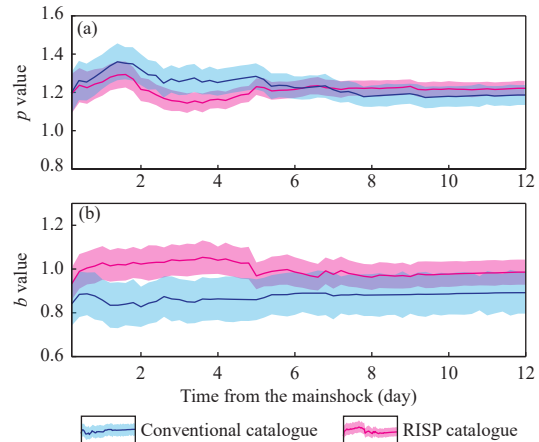


Figure 6. Parameters of Omi-R-J model against the duration time (since the mainshock occurred) in fitting the $M_w 5.5$ Pingyuan earthquake sequence based on conventional and RISP catalogue. (a) represents p value change based on conventional and RISP catalogue, (b) represents b value change based on conventional and RISP catalogue respectively. The shaded area shows the range of the standard deviations of the parameters shown in each subgraph.

and p in the stable period are similar, but because RISP detects more small events in initial stage, the sequence attenuation is relatively slow, and the amplitude change of p value is smaller than the conventional catalogue. Due to the lack of small earthquakes in the early aftershock window, the b value is relatively low in the conventional catalogue. In the catalog created by RISP, small earthquake events below $M_L 2.0$ are supplemented, so that the sequence parameters can more objectively reflect the development characteristics of the parameter sequence. Compared with the conventional catalogue, the aftershock sequence by the RISP has higher monitoring ability, which can quickly obtain stable sequence parameters after the mainshock, and play a greater role in post-earthquake emergency and disaster assessment.

4.2. Focal mechanism solution

The mainshock was well recorded by regional seismic stations from China National Seismic Network (Zheng XF et al., 2010). To determine the double-couple solution of the mainshock, we employed the “Cut-and-Paste (CAP)” algorithm (Zhao LS and Helmberger, 1994; Zhu LP and Helmberger, 1996) assuming a spatial point source. In the waveform inversion, we analyzed the broadband waveforms of regional seismograms from 16 stations within 220 km of the epicenter. The PnL and surface wave segments were band-pass filtered at 0.02–0.15 Hz and 0.02–0.10 Hz, respectively. For the computation of Green’s functions, we employed frequency-wavenumber (F-K)

technique (Zhu LP and Rivera, 2002) based on the 1-D velocity model derived from the deep seismic sounding result (Duan YH et al., 2016).

The focal mechanism solutions are calculated over a range of depths to identify the depth with the minimum misfit between the observed and synthetic waveforms. As displayed in Figure 7, the best waveform match is achieved at the depth of 20 km with an estimated magnitude $M_w 5.5$, which is consistent with the Global CMT results ($M_w 5.6$). The relatively high cross-correlation coefficients between the synthetics and observed data suggest that the source parameters are well resolved. Showing oblique-normal faulting, the focal mechanism implies that the strike, dip, and rake are $226^\circ/65^\circ/-166^\circ$, respectively, with an auxiliary nodal plane solution of $130^\circ/77^\circ/-26^\circ$. Our focal mechanism solution and centroid depth are also consistent with those published by the CENC (<https://news.ceic.ac.cn>), Global CMT Project (www.globalcmt.org/CMTsearch.html) and Zhang Z et al (2024) (Table 1).

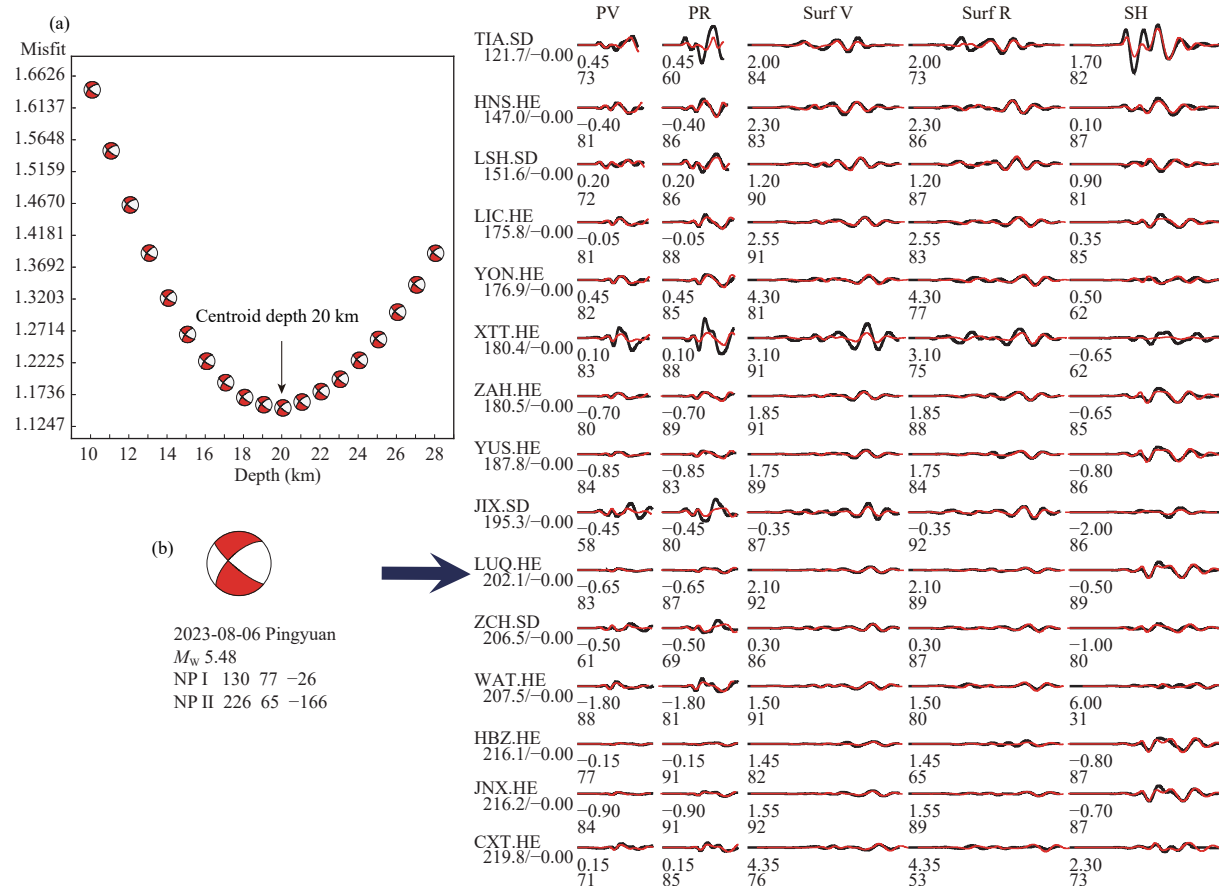


Figure 7. Focal mechanism solution of Pingyuan $M_w 5.5$ earthquake. (a) The misfit as a function of centroid depth. (b) Comparison between observed (black) and synthetic (red) seismograms. The numbers below the station names are the epicenter distances in kilometers. The first number below each seismogram is the time shift between data and synthetics and the second number is the cross-correlation coefficient in percentage.

5. Discussion

5.1. Seismogenic fault

The long axes of spatial distribution of both PGA and PGV strike along the northeast direction (Figure 3). Furthermore, locations of the earthquake sequence distribution suggest that the aftershocks primarily trend along NE above the mainshock, with a high angle ($\sim 63^\circ$) dipping to NW (Figure 5). In addition, the focal mechanism solution indicates that the Pingyuan $M_w 5.5$ earthquake is a strike-slip event with a normal component. Consistent with the distribution of PGA, PGV, and aftershocks, the nodal plane strikes along 226° and dips to NW at an angle of about 65° (Figure 7). Integrating with the regional structures, the GTF and LTF are the only two faults that activated in Pleistocene near the epicenter (Figure 1b) with a similar NE trending and 60° – 80° dip angle (Jia HY and Liu XL 2019; Ma SZ, 2007), showing a strong connection with this event. However, there is no surface rupture or

Table 1. Pingyuan M_W 5.5 earthquake focal mechanism solutions.

Agency/Author	Nodal plane I	Nodal Plane II	Depth (km)	M_W
	Strike (°)/Dip (°)/Rake (°)	Strike (°)/Dip (°)/Rake (°)		
CENC	123/62/-24	225/69/-150	11.0	5.5
USGS	37/70/-171	304/81/-21	11.5	5.4
GCMT	125/69/-17	221/74/-158	18.0	5.6
GFZ	127/87/-13	217/76/-177	15.0	5.5
Zhang Z et al. (2024)	126/70/-16	222/75/-160	16.0	5.5
This study	130/77/-26	226/65/-166	20.0	5.5

Note: CENC: China Earthquake Networks Center (<https://news.ceic.ac.cn>); USGS: United States Geological Survey (<https://www.usgs.gov>); GCMT: the Global Centroid Moment Tensor project (<https://www.globalcmt.org>); GFZ: the GFZ German Research Centre for Geosciences (<https://geofon.gfz-potsdam.de>).

previously activated faults in the Quaternary between the GTF and LTF faults where the epicenter is located. Therefore, it is reasonable to infer that a blind fault connecting the GTF and LTF faults at depth is responsible for the M_W 5.5 Paingyuan earthquake, considering the majority of aftershocks occurring at depths of 15–20 km. Notably, the GTF and LTF faults were previously regarded as inactive faults in the Holocene (Liu TT and Hua AJ, 2007). Therefore, this seismic activity highlights the potential of high seismic hazards along the GTF and LTF in the future.

5.2. S-velocity structure beneath NCP

The S-wave velocity (v_S) model used in this study is derived from Huang X et al. (2023), which is obtained using joint inversion of Rayleigh wave phase velocity and ellipticity. These two datasets are derived from ambient noise cross-correlation and teleseismic earthquake waveforms recorded by ChinArray-III. There were more than 600 portable broadband stations (two stages) deployed in North China from 2016 to 2020 with an average station spacing of ~35 km. Rayleigh wave phase velocity and ellipticity are jointly inverted for 1D v_S models using a Bayesian Markov chain Monte Carlo (MCMC) method. The 1D models are parameterized with three layers, consisting of a sedimentary, a crystal crustal, and an upper mantle layer. Specific details can be referred to Huang et al. (Huang X et al., 2021; 2023). As the crustal thickness is one of the independent parameters, the distribution of crustal thickness can be obtained after inversion.

We present a horizontal slice at 20 km depth and a vertical profile crossing the seismic source zone of the 3D v_S model (Figure 8). The horizontal slice of the v_S model reveals that the mainshock is located at the junction of high and low-velocity anomaly (Figure 8a). Moreover, the

vertical profile of the v_S model indicates that the crustal thickness at the location of the mainshock is ~33 km (Figure 8b, white dashed line), significantly thinner than the surrounding areas. This observation suggests a local uplift of the Moho beneath the mainshock zone, potentially linked to the occurrence of the Pingyuan earthquake sequence. Huang X et al. (2023) primarily attribute the crustal modification and thinning in this area to the thermal-chemical erosion caused by magma upwelling. Therefore, it suggests that the seismic activity in this area may be related by the upwelling of magma from the upper mantle.

5.3. Tectonic implication and seismic hazard

During Late Mesozoic, the NCC underwent significant tectonic deformation and magmatism in large scale, resulting in the reduction in stability (Zhu RX et al., 2011, 2012; Zhang SH et al., 2014). In the Cenozoic, the NCC lithosphere was destroyed at depths of ~45–55 km, leading to the formation of extensive basins (Li SZ et al., 2012; Wang GZ et al., 2022), as well as the tectonic background for seismicity in the NCP. Strong earthquakes have occurred in the NCP over the past century. Focal mechanism solutions suggest that these seismogenic faults primarily exhibit strike-slip movement, occasionally with a small number of reverse or normal components (Wu MJ et al., 2011; Zhang YG et al., 2018). The maximum principal compressive stress axis trends NE-NEE, while the minimum stress axis aligns NW-NNW (Wu MJ et al., 2011). Based on contemporary deformation data from the Global Positioning System (GPS), Zhang YG et al. (2018) proposed that the NNE-NE trending strike-slip active faults developed to accommodate the left-lateral deformation between the Amurian and South China blocks.

P-wave velocity vertical profiles indicate the presence of a high-velocity zone in the lower crust along deep-

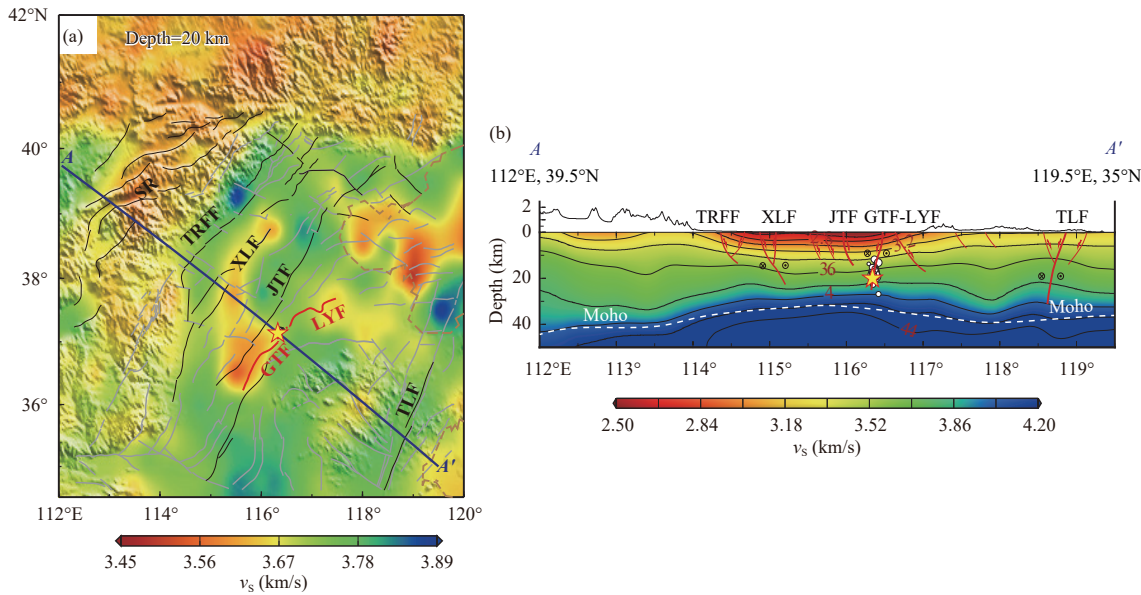


Figure 8. S-wave velocity (v_s) model in the NCP (modified after from Huang X et al., 2023). (a) S-wave velocity slices at the depth of 20 km, in which the mainshock occurred. (b) Vertical profile of the v_s model across the active faults in NCP with the mainshock and aftershocks of the 2023 M_w 5.5 Pingyuan Earthquake. The white dashed line represents the crustal thickness. SR: Shanxi rift; TRFF: Taihang range front fault; XLF: Xingtai-Langfang fault; JTF: Jixian-Tangshan fault; GTF: Gaotang fault; LYF: Lingxian-Yangxin fault; TLF: Tan-Lu fault.

seated faults beneath the NCP, such as the ZBFZ and TLF (Hao TY et al., 2013). This high-velocity zone, possibly related to diapirism magma, is considered to originate from the dehydration and melting of subducted ancient Pacific plate slabs (Figure 9, Wang GZ et al., 2022). Our S-wave velocity vertical profiles (Figure 8b) also reveal a similar structure, with a shallower depth of the Moho beneath the NCP, possibly contributed by the uprising of hot material (Figure 9). These deep thermal activities are considered significant in generating strong earthquakes within the NCP (Deng QD et al., 2003). In areas with crustal non-homogeneities, stress-strain energy tends to concentrate from softer magma to harder inclusions. Consequently, changes in stress concentration are more likely to occur in the contact areas between deep faults and softer materials, eventually leading to fault instability and occurrence of earthquake (Xiao LX et al., 1999). By analyzing the geometry of seismogenic faults and deep structures, the underneath hot material is believed to have played a significant role in the occurrence of the 1966 $M_7.2$ Xingtai earthquake and 1976 $M_7.6$ Tangshan earthquake (Wang CY et al., 1997; Xiao LX et al., 1999; Li ZW et al., 2018; Li HL et al., 2022; Zhang GW et al., 2022; Cai JT et al., 2023). Therefore, combining with the tectonic deformation and deep structure, we propose that the Pingyuan earthquake is likely resulted by the combined effects of shear deformation between the Amurian and South China blocks and the uplift of deep hot materials.

Despite the historical damaging earthquakes in the

NCP, no earthquakes larger than $M_6.0$ have been recorded since 1976 (CENC, <http://www.ceic.ac.cn/history>). Within the last two decades, only three earthquakes with magnitude larger than 5.0 have occurred, namely the 2006 Wen'an M_S 5.1 earthquake, the 2020 Tangshan M_S 5.1 earthquake, and the 2023 M_W 5.5 Pingyuan earthquake (<http://www.ceic.ac.cn/history>). The presence of thick sedimentary layers, estimated to be around 4–6 km in depth (Huang X et al., 2023), poses challenges in identifying the seismogenic fault within the NCP. Consequently, it is imperative to conduct further investigations and quantitative research on active faults to enhance our understanding of the seismotectonic characteristics beneath the NCP. Additionally, it is also vital to investigate the local stress characteristics of large strike-slip faults and explore the coupling relationship between deep and shallow deformation processes.

6. Conclusions

In this study, we analyzed strong ground motion records, aftershock sequence relocation, focal mechanism of the mainshock and geological data to understand the seismotectonics of the Pingyuan earthquake. We have reached the following conclusions:

(1) The aftershocks of the M_W 5.5 Pingyuan earthquake trends NE with a total length of ~9 km and dips NW at an angle of ~63°, revealing the seismogenic fault plane

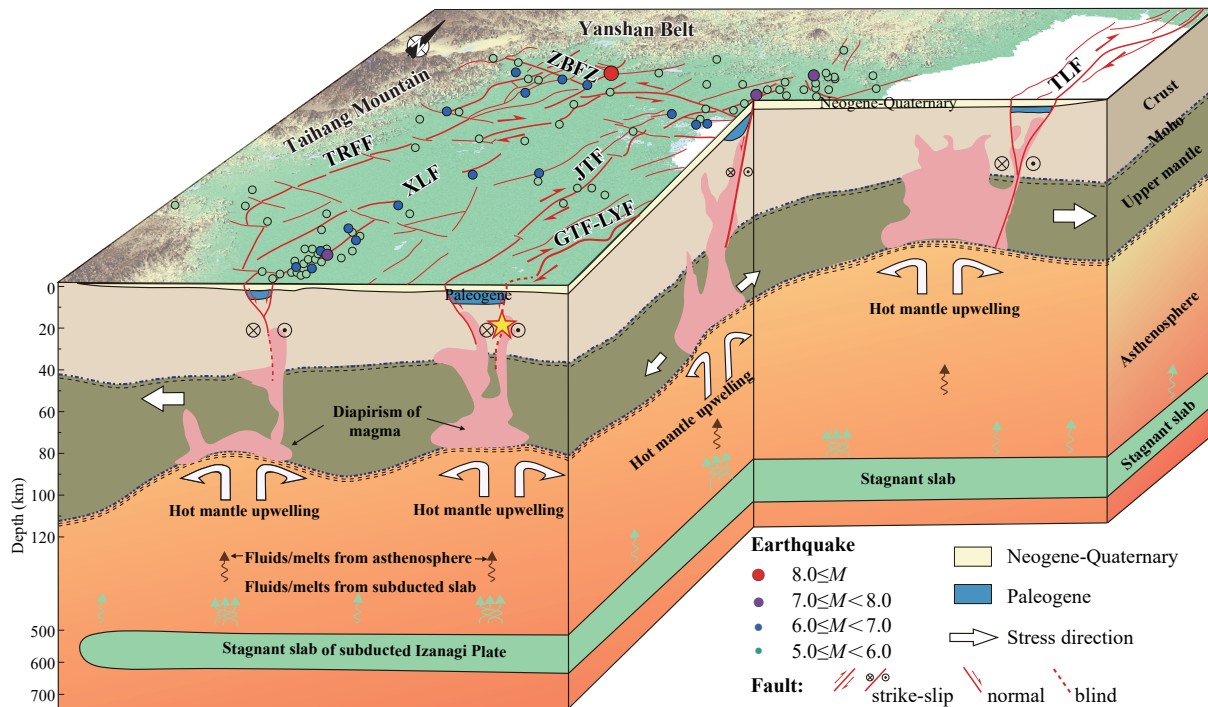


Figure 9. Conceptual seismotectonic model showing the active faults and deep deformation interpretations in the NCP. Yellow pentagram represents the epicenter of Pingyuan $M_{\text{W}} 5.5$ earthquake. Active faults are revised from Zhang YG et al. (2018). Interpretation of crustal and asthenosphere deformation is modified after Qi JF and Yang Q (2010), and Wang GZ et al. (2022). TRFF: Taihang range front fault; ZBFZ: Zhangjiakou-Bohai fault zone; XLF: Xingtai-Langfang fault; JTF: Jixian-Tangshan fault; GTF-LYF: Gaotang fault and Lingxian-Yangxin fault; TLF: Tan-Lu fault.

(226°/65°–166°), which was resolved from focal mechanism solutions.

(2) The observed horizontal PGAs and PGVs generally ranges between 200–300 cm/s² and 10–20 cm/s, resulting a significant near-field saturation phenomenon within a 30 km.

(3) Combining with the earthquake sequence, distribution of strong ground motion, as well as the velocity structure, we suggest that a blind fault between the Guantao fault and the Lingxian-Yangxian fault was responsible for the generation of the Pingyuan earthquake, which was probably resulted by the combined effects of shear strain between the Amurian and South China blocks and the uplift of deep hot materials.

(4) Further investigation and detection of deep active faults, as well as detailed interpretation of deep structures beneath the NCP are crucial to enhance our understanding of seismic hazards in the deep sedimentary covering regions.

Acknowledgments

Waveform data for this study were provided by Data Management Centre of China National Seismic Network at

Institute of Geophysics, China Earthquake Administration. The earthquake bulletins were provided by Tengchao Dong and Shirong Liao. This research was jointly supported from the National Natural Science Foundation of China (No. 42374081), the Fundamental Research Funds for the Institute of Geophysics, China Earthquake Administration (Nos. DQJB23B22, DQJB22K36 and DQJB23Q04), and Hong Research Grants Council (Nos. 14306122 and 14308523).

Conflict of interest

Prof. Hongfeng Yang and Prof. Lihua Fang serve as editorial board members for *Earthquake Science* and were not involved in the editorial review or the decision-making process for this article. All authors declare that they have no competing interests.

References

- Abrahamson NA, Silva WJ and Kamai R (2014). Summary of the ASK14 ground motion relation for active crustal regions. *Earthq Spectra* **30**(3): 1025–1055. <https://doi.org/10.1193/070913EQS198M>.
- Bi JM, Jiang CS, Lai GJ and Song C (2022). Effectiveness

- evaluation and constraints of early aftershock probability forecasting for strong earthquakes in continental China. *Chin J Geophys* **65**(7): 2532–2545. <https://doi.org/10.6038/cjg2022P0411> (in Chinese with English abstract).
- Boore DM, Stewart JP, Seyhan E and Atkinson GM (2014). NGA-West2 equations for predicting PGA, PGV and 5% damped PSA for shallow crustal earthquakes. *Earthq Spectra* **30**(3): 1057–1085. <https://doi.org/10.1193/070113EQS184M>.
- Cai JT, Chen XB, Dong ZY, Zhan Y, Liu ZY, Cui TF and Jiang F (2023). Three-dimensional electrical structure beneath the epicenter zone and seismogenic setting of the 1976 M_s 7.8 Tangshan earthquake, China. *Geophys Res Lett* **50**(14): e2022 GL102291. <https://doi.org/10.1029/2022GL102291>.
- Campbell KW and Bozorgnia Y (2014). NGA-West2 ground motion model for the average horizontal components of PGA, PGV and 5% damped linear acceleration response spectra. *Earthq Spectra* **30**(3): 1087–1115. <https://doi.org/10.1193/062913EQS175M>.
- Chiou BSJ and Youngs RR (2014). Update of the Chiou and Youngs NGA model for the average horizontal component of peak ground motion and response spectra. *Earthquake Spectra* **30**(3): 1117–1153. <https://doi.org/10.1193/072813EQS219M>.
- Dai DQ and Xi N (2023). Rapid inversion of the rupture process of the $M_{5.5}$ earthquake in Shandong Pingyuan on August 6, 2023. *Earthquake Res China* **39**(3): 659–694. <https://doi.org/10.3969/j.issn.1001-4683.2023.03.019> (in Chinese with English abstract).
- Deng QD, Zhang PZ, Ran YK, Yang XP, Min W and Chu QZ (2003). Basic characteristics of active tectonics of China. *Sci China Ser D Earth Sci* **46**(4): 356–372. <https://doi.org/10.1360/03yd9032>.
- Duan YH, Wang FY, Zhang XK, Lin JY, Liu Z, Liu BF, Yang ZX, Guo WB and Wei YH (2016). Three-dimensional crustal velocity structure model of the middle-eastern north China Craton (HBCrust1.0). *Sci China Earth Sci* **59**(7): 1477–1488. <https://doi.org/10.1007/s11430-016-5301-0>.
- Fan LP, Li BR, Liao SR, Jiang C and Fang LH (2022). High-precision relocation of the aftershock sequence of the January 8, 2022, M_s 6.9 Menyuan earthquake. *Earthq Sci* **35**(2): 138–145. <https://doi.org/10.1016/j.eqs.2022.01.021>.
- Fang LH, Wu JP, Wang WL, Du WK, Su JR, Wang CZ, Yang T and Cai Y (2015). Aftershock Observation and Analysis of the 2013 M_s 7.0 Lushan Earthquake. *Seismol Res Lett* **86**(4): 1135–1142. <https://doi.org/10.1785/0220140186>.
- Gao S, Rudnick RL, Carlson RW, McDonough WF and Liu YS (2002). Re-Os evidence for replacement of ancient mantle lithosphere beneath the North China Craton. *Earth Planet Sci Lett* **198**(3-4): 307–322. [https://doi.org/10.1016/S0012-821X\(02\)00489-2](https://doi.org/10.1016/S0012-821X(02)00489-2).
- Guo H, Jiang WL and Xie XS (2011). Late-Quaternary strong earthquakes on the seismogenic fault of the 1976 M_s 7.8 Tangshan earthquake, Hebei, as revealed by drilling and trenching. *Sci China Earth Sci* **54**(11): 1696–1715. <https://doi.org/10.1007/s11430-011-4218-x>.
- Guo H and Zhao JX (2019). The surface rupture zone and paleoseismic evidence on the seismogenic fault of the 1976 M_s 7.8 Tangshan earthquake, China. *Geomorphology* **327**: 297–306. <https://doi.org/10.1016/j.geomorph.2018.11.006>.
- Hao TY, You QY, Liu LH, Lv CC, Xu Y, Li ZW, Zhao CL, Zheng YP, Liu CG and Han GZ (2013). Joint land-sea seismic survey and research on the deep structures of the Bohai Sea areas. *Acta Oceanol Sin* **32**(12): 13–24. <https://doi.org/10.1007/s13131-013-0383-4>.
- Huang X, Ding ZF, Ning JY, Niu FL, Li GL, Wang XC and Xu XM (2021). Sedimentary and crustal velocity structure of Trans-North China Orogen from joint inversion of Rayleigh wave phase velocity and ellipticity and some implication for Syn-rift volcanism. *Tectonophysics* **819**: 229–104. <https://doi.org/10.1016/j.tecto.2021.229104>.
- Huang X, Wang WT and Ding ZF (2023). Sedimentary and crustal structure of eastern North China from joint inversion of Rayleigh wave phase velocity and ellipticity and its implication for magmatism. *Tectonophysics* **846**: 229–680. <https://doi.org/10.1016/j.tecto.2022.229680>.
- Jia HY and Liu XL (2019). Evolution mechanism of faults in northern boundary of Huimin sag. *Pet Geophys* **17**(4): 59–67 (in Chinese with English abstract).
- Jiang PF (2022). Simulation of historical strong earthquake recurrence in Beijing, Tianjin and Hebei regions and analysis of disaster losses. Dissertation. Institute of Engineering Mechanics, China Earthquake Administration, Harbin, pp 1–68. <https://doi.org/10.27490/d.cnki.ggjgy.2022.000082> (in Chinese with English abstract).
- Li HL, Tian Y, Zhao DP and Yan D (2022). Anatomy of large earthquakes in North China. *J Asian Earth Sci* **237**: 105342. <https://doi.org/10.1016/j.jseas.2022.105342>.
- Li SZ, Zhao GC, Dai LM, Zhou LH, Liu X, Suo YH and Santosh M (2012). Cenozoic faulting of the Bohai Bay Basin and its bearing on the destruction of the eastern North China Craton. *J Asian Earth Sci* **47**: 80–93. <https://doi.org/10.1016/j.jseas.2011.06.011>.
- Li ZW, Ni SD, Roecker S, Bao F, Wei X and Yuen DA (2018). Seismic imaging of source region in the 1976 M_s 7.8 Tangshan earthquake sequence and its implications for the seismogenesis of intraplate earthquakes. *Bull Seismol Soc Am* **108**(3A): 1302–1313. <https://doi.org/10.1785/0210170389>.
- Liao SR, Zhang HC, Fan LP, Li BR, Huang LZ, Fang LH and Qin M (2021). Development of a real-time intelligent seismic processing system and its application in the 2021 Yunnan Yangbi M_s 6.4 earthquake. *Chin J Geophys* **64**(10): 3632–3645. <https://doi.org/10.6038/cjg2021O0532> (in Chinese with English abstract).
- Lin W, Faure M, Monié P, Schärer U and Panis D (2008). Mesozoic extensional tectonics in eastern Asia: the South Liaodong Peninsula Metamorphic Core Complex (NE China). *J Geol* **116**(2): 134–154. <https://doi.org/10.1086/527456>.
- Liu M, Stein S and Wang H (2011). 2000 years of migrating

- earthquakes in North China: how earthquakes in midecontinents differ from those at plate boundaries. *Lithosphere* **3**(2): 128–132. <https://doi.org/10.1130/L129.1>.
- Liu TT and Hua AJ (2007). Preliminary study on seismic geology and activity in Jinan area. In: Zang SX ed. Proceedings of the 23rd Annual Conference of the Chinese Geophysical Society 18. China Ocean University Press, Qingdao, China, pp 553 (in Chinese).
- Ma SZ (2007). The study of Paleogene tectonic-sedimentary evolution and hydrocarbon reservoir formation model in Huimin sag. Dissertation. China University of Geosciences (Beijing): Beijing, pp 1–166 (in Chinese with English abstract).
- Meng QR (2003). What drove late Mesozoic extension of the northern China-Mongolia tract? *Tectonophysics* **369**(3-4): 155–174. [https://doi.org/10.1016/S0040-1951\(03\)00195-1](https://doi.org/10.1016/S0040-1951(03)00195-1).
- Ogata Y and Katsura K (1993). Analysis of temporal and spatial heterogeneity of magnitude frequency distribution inferred from earthquake catalogues. *Geophys J Int* **113**: 727–738. <https://doi.org/10.1111/j.1365-246X.1993.tb04663.x>.
- Omi T, Ogata Y, Hirata Y and Aihara K (2013). Forecasting large aftershocks within one day after the main shock. *Sci Rep* **3**: 2218. <https://doi.org/10.1038/srep02218>.
- Qi JF and Yang Q (2010). Cenozoic structural deformation and dynamic processes of the Bohai Bay basin province, China. *Mar Pet Geol* **27**(4): 757–771. <https://doi.org/10.1016/j.marpetgeo.2009.08.012>.
- Qiu HB, Lin W, Chen Y and Faure M (2023). Jurassic-Early Cretaceous tectonic evolution of the North China Craton and Yanshanian intracontinental orogeny in East Asia: new insights from a general review of stratigraphy, structures and magmatism. *Earth Sci Rev* **237**: 104320. <https://doi.org/10.1016/j.earscirev.2023.104320>.
- Reasenberg PA and Jones LM (1989). Earthquake hazard after a mainshock in California. *Science* **243** (4895): 1173–1176. <https://doi.org/10.1126/science.243.4895.1173>.
- Waldhauser F and Ellsworth WL (2000). A double-difference earthquake location algorithm: method and application to the northern Hayward fault, California. *Bull Seismol Soc Am* **90**(6): 1353–1368. <https://doi.org/10.1785/0120000006>.
- Wang CY, Zhang XK, Lin ZY, Wu QJ and Zhang YS (1997). Crustal structure beneath the Xingtai earthquake area in North China and its tectonic implications. *Tectonophysics* **274**(4): 307–319. [https://doi.org/10.1016/S0040-1951\(97\)0006-1](https://doi.org/10.1016/S0040-1951(97)0006-1).
- Wang CY, Wu QJ, Duan YH, Wang ZS and Lou H (2017). Crustal and upper mantle structure and deep tectonic genesis of large earthquakes in North China. *Sci China Earth Sci* **60**(5): 821–857. <https://doi.org/10.1007/s11430-016-9009-1>.
- Wang GZ, Li SZ, Suo YH, Zhang XQ, Zhang Z, Wang DY, Liu Z, Liu YJ, Zhou J, Wang PC and Guo LL (2022). Deep-shallow coupling response of the Cenozoic Bohai Bay Basin to plate interactions around the Eurasian Plate. *Gondwana Res* **102**: 180–199. <https://doi.org/10.1016/j.gr.2020.09.002>.
- Wang T, Zheng YD, Zhang JJ, Zeng LS, Donskaya T, Guo L and Li JB (2011). Pattern and kinematic polarity of late Mesozoic extension in continental NE Asia: perspectives from metamorphic core complexes. *Tectonics* **30**(6): TC6007. <https://doi.org/10.1029/2011tc002896>.
- Wiemer S and Katsumata K (1999). Spatial variability of seismicity parameters in aftershocks zones. *J Geophys Res: Solid Earth* **104**(13): 13 135–13 151. <https://doi.org/10.1029/1999JB900032>.
- Wu MJ, Lin XD and Xu P (2011). Analysis of focal mechanism and tectonic stress field features in northern part of North China. *J Geod Geodyn* **31**(5): 39–43. <https://doi.org/10.3969/j.issn.1671-5942.2011.05.009> (in Chinese with English abstract).
- Xiao LX, Zhu YQ, Zhang SQ, Liu X and Guo Y (1999). The relationship between the deep-level structure in crust and brewing of strong earthquakes in Xingtai area. *Acta Seismol Sin* **12**(6): 647–658. <https://doi.org/10.1007/s11589-999-0065-7>.
- Xie JJ, Zimmaro P, Li XJ and Wen ZP (2017). Rupture directivity effects on strong ground motion during the 15 April 2016 M_W 7.0 Kumamoto earthquake in Japan. *Bull Seismol Soc Am* **107**(3): 1265–1276. <https://doi.org/10.1785/0120160258>.
- Xie JJ, Wang WC, An Z, Li KW, Tian XF, Wu LN, Gao SD, Zhang WD and Yuan J (2023). Quantification of rupture directivity effects on strong ground motion during the 8 January 2022 M_S 6.9 Menyuan earthquake in Qinghai, China. *Front Earth Sci* **10**: 1068536. <https://doi.org/10.3389/feart.2022.1068536>.
- Xu J, Niu LF, Wang CH and Han ZJ (1996). Tangshan-Hejian-Cixian newly-generated seismotectonic zone. *Seismol Geol* **18**(3): 193–198 (in Chinese with English abstract).
- Xu W, Qiu NS, Wang Y and Chang J (2018). Evolution of Meso-Cenozoic lithospheric thermal-rheological structure in the Jiyang sub-basin, Bohai Bay Basin, eastern North China Craton. *Int J Earth Sci* **107**(1): 153–166. <https://doi.org/10.1007/s00531-016-1360-x>.
- Xu W, Qiu NS and Li Y (2019). Evolution of the Cenozoic thermal lithosphere of the Jiyang Sub-basin, Bohai Bay Basin: implications for the lithospheric thinning mechanism. *Tectonophysics* **773**: 228–229. <https://doi.org/10.1016/j.tecto.2019.228229>.
- Yao SL and Yang HF (2023). Towards ground motion prediction for potential large earthquakes from interseismic locking models. *Earth Planet Sci Lett* **601**: 117905. <https://doi.org/10.1016/j.epsl.2022.117905>.
- Yin XF, Zhang GM, Shao ZG, Wang P and Sun XZ (2020). Research on activity characteristics of strong earthquakes in North China. *Earthquake* **40**(1): 11–33. <https://doi.org/10.12196/j.issn.1000-3274.2020.01.002> (in Chinese with English abstract).
- Yu FS and Koyi H (2016). Cenozoic tectonic model of the Bohai Bay Basin in China. *Geol Mag* **153**(5-6): 866–886. <https://doi.org/10.1017/S0016756816000492>.
- Yu ZY, Pan H, Xi H, Zhang YH and Chen H (2019). Late

- Quaternary paleoseismicity of the Xiadian fault in the North China Plain with implications for earthquake potential. *J Asian Earth Sci* **184**: 103 997. <https://doi.org/10.1016/j.jseas.2019.103997>.
- Zhang GW, Ji Y, Guo H and Hu XP (2022). Complex fault geometry of the 1976 $M_{\text{S}}7.8$ Tangshan earthquake source region in North China. *Tectonophysics* **845**: 229 642. <https://doi.org/10.1016/j.tecto.2022.229642>.
- Zhang L, Zhou YJ, Zhang X, Zhu AY, Wang SG, Liang SS, Jiang C, Wu JP, Li YX, Su JR, Yan LJ and Fang LH (2023). 2022 $M_{\text{W}}6.6$ Luding, China, Earthquake: a strong continental event illuminating the Moxi seismic gap. *Seismol Res Lett* **94**(5): 2 129–2 142. <https://doi.org/10.1785/0220220383>.
- Zhang PZ, Deng QD, Zhang ZQ and Li HB (2013). Active faults, earthquake hazards and associated geodynamic processes in continental China. *Sci Sinica Terra* **43**(10): 1 607–1 620 (in Chinese). <https://doi.org/10.1360/zd-2013-43-10-1607>.
- Zhang SH, Zhao Y, Davis GA, Ye H and Wu F (2014). Temporal and spatial variations of Mesozoic magmatism and deformation in the North China Craton: implications for lithospheric thinning and decratonization. *Earth Sci Rev* **131**: 49–87. <https://doi.org/10.1016/j.earscirev.2013.12.004>.
- Zhang YG, Zheng WJ, Wang YJ, Zhang DL, Tian YT, Wang M, Zhang ZQ and Zhang PZ (2018). Contemporary deformation of the North China plain from global positioning system data. *Geophys Res Lett* **45**(4): 1 851–1 859. <https://doi.org/10.1002/2017GL076599>.
- Zhang YX, Dai DQ, Yang ZG, Xi N, Zhang JY, Han GJ, Xu TR, Deng WZ and Sun L (2023). Preliminary analysis of source parameters of the $M_{\text{S}}5.5$ earthquake on August 6, 2023 in Pingyuan country, Shandong province. *Earthquake Res China* **39**(4): 902–912. <https://doi.org/10.3969/j.issn.1001-4683.2023.04.017> (in Chinese with English abstract).
- Zhang Z, Xu LS and Fang LH (2024). The $M_{\text{W}}5.5$ earthquake on August 6, 2023, in Pingyuan, Shandong, China: a rupture on a buried fault. *Earthq Sci* **37**(1): 1–12. <https://doi.org/10.1016/j.eqs.2023.10.001>.
- Zhang ZL, Li QZ, Gu JC, Jin YM, Yang MY and Liu WQ (1980). The fracture processes of the Tangshan earthquake and its mechanical analysis. *Acta Seismol Sin* **2**(2): 111–129 (in Chinese with English abstract).
- Zhao C, Zhao CP, Lei HF and Yao MD (2022). Seismic activities before and after the impoundment of the Xiangjiaba and Xiluodu reservoirs in the lower Jinsha River. *Earthq Sci* **35**(5): 355–370. <https://doi.org/10.1016/j.eqs.2022.10.003>.
- Zhao LS and Helmberger DV (1994). Source estimation from broadband regional seismograms. *Bull Seismol Soc Am* **84**(1): 91–104. <https://doi.org/10.1785/BSSA0840010091>.
- Zheng G, Wang H, Wright TJ, Lou YD, Zhang R, Zhang WX, Shi C, Huang JF and Wei N (2017). Crustal deformation in the India-Eurasia collision zone from 25 years of GPS measurements. *J Geophys Res: Solid Earth* **122**(11): 9 290–9 312. <https://doi.org/10.1002/2017JB014465>.
- Zheng XF, Yao ZX, Liang JH and Zheng J (2010). The role played and opportunities provided by IGP DMC of China National Seismic Network in Wenchuan earthquake disaster relief and researches. *Bull Seismol Soc Am* **100**(5B): 2 866–2 872. <https://doi.org/10.1785/0120090257>.
- Zhu G, Chen Y, Jiang DZ and Lin SZ (2015). Rapid change from compression to extension in the North China Craton during the Early Cretaceous: evidence from the Yunmengshan metamorphic core complex. *Tectonophysics* **656**: 91–110. <https://doi.org/10.1016/j.tecto.2015.06.009>.
- Zhu LP and Helmberger DV (1996). Advancement in source estimation techniques using broadband regional seismograms. *Bull Seismol Soc Am* **86**(5): 1 634–1 641. <https://doi.org/10.1785/BSSA0860051634>.
- Zhu LP and Rivera LA (2002). A note on the dynamic and static displacements from a point source in multilayered media. *Geophys J Int* **148**(3): 619–627. <https://doi.org/10.1046/j.1365-246X.2002.01610.x>.
- Zhu RX, Chen L, Wu FY and Liu JL (2011). Timing, scale and mechanism of the destruction of the North China Craton. *Sci China Earth Sci* **54**(6): 789–797. <https://doi.org/10.1007/s11430-011-4203-4>.
- Zhu RX, Yang JH and Wu FY (2012). Timing of destruction of the North China Craton. *Lithos* **149**: 51–60. <https://doi.org/10.1016/j.lithos.2012.05.013>.
- Zhu WQ and Beroza GC (2019). PhaseNet: a deep-neural-network-based seismic arrival-time picking method. *Geophys J Int* **216**(1): 261–273. <https://doi.org/10.1093/gji/ggy423>.